JOURNAL OF MATERIALS SCIENCE 25 (1990) 1645–1655

Transmission electron microscopy of second-phase particles in $Pb(Sc_{1/2}Ta_{1/2})O_3$ Ferroelectric ceramics

K. Z. BABA-KISHI, I. M. REANEY, D. J. BARBER
Physics Department, University of Essex, Colchester CO4 3SQ, UK

Pb-rich second-phase particles in perovskite-structured $Pb(Sc_{1/2}Ta_{1/2})O_3$ (PST) ferroelectric ceramic relaxors have been investigated using transmission electron microscopy. The second-phase particles were observed to exhibit a range of morphologies which included spheroidal inclusions, plate-like precipitates and intergranular films. Moiré fringes and lattice images have been used to identify various non-perovskite phases. It is deduced that excess PbO, which is used to assist densification through liquid phase sintering and to promote grain growth, becomes entrapped within the ceramics, thereby producing Pb-enriched phases that have adverse effects on dielectric properties.

1. Introduction

The perovskite-structured relaxor lead scandium tantalate, $Pb(Sc_{1/2}Ta_{1/2})O_3$ (PST), is an important member of a special class of ferroelectric compounds (for example, $Pb_{0.88}La_{0.08}(Zr_{0.70}Ti_{0.03})O_3$ which possess reversible electric dipoles. These compounds exhibit broad ferroelectric–paraelectric (FE–PE) phase transitions which are believed to originate from micro-scale chemical inhomogeneities, so that both the dielectric permittivity and the spontaneous polarization change slowly over a 'Curie temperature range' and not at a well-defined temperature (Curie point) [1–3]. These so-called relaxor materials also exhibit a high dielectric permittivity which has led to their use in various electronic devices. Thus microstructural control over dielectric properties and the achievement of optimum dielectric behaviour has important practical implications.

Several workers have investigated the microstructure of PST (prepared by sintering mixed oxides) using transmission electron microscopy (TEM) [4, 5]. The compound conforms to the general formula $A(B'_xB''_{1-x})O_3$ with the Pb-ions occupying the A-sites and the Sc and Ta ions located on the B-site lattice (Fig. 1). The unit cell of the material has the perovskite ($CaTiO_3$) structure, which can be envisaged as BO_6 octahedra centred on the corners of a simple cube linked together by the sharing of oxygen ions. The A-site cation occupies the centre of the cube. Distortion of this cubic structure at the PE–FE transition gives rise to a spontaneous electric dipole within the unit cell, parallel to a $\langle 1\,1\,1 \rangle$ direction.

Electron diffraction studies have shown that heat treatment promotes ordering of the B-site cations within PST, resulting in the formation of a face-centred cubic superlattice ($2a_0\,2a_0\,2a_0$) (see Section 4) [2, 5]. The Bragg reflections within the electron diffraction patterns which arise from the face-centred array of scandium and tantalum ions are often referred to as F-spots. Dark-field images obtained using F-spots have revealed ordered domains that appear to have enlarged preferentially at grain boundaries and planar defects [6]. The average size of the ordered domains is dependent upon the heat treatment given subsequent to fabrication.

The degree of structural order is known to influence the dielectric behaviour of relaxor compounds [5]. In addition, microstructural characteristics such as grain size, grain boundary area, grain shape, porosity, the presence of lead-based pyrochlore-structured parasite phases and other non-perovskite second-phase particles are considered to be important factors influencing dielectric properties, e.g. permittivity and loss.

Owing to the volatile nature of PbO, Pb-based relaxor ferroelectric oxide ceramics are now commonly fabricated by the 'Columbite' or 'Wolframite' method (see Section 2.1.) which inhibits the formation of the parasite pyrochlore-type phases. It is now also possible to prepare the ceramic precursors by sol methods, enabling greater structural homogeneity to be achieved in the sintered product. The addition of excess PbO (typically 5 to 10 wt %) prior to sintering is also beneficial, since it suppresses the formation of pyrochlore-structured second-phase and aids densification by means of liquid-phase sintering. However, the idea that other Pb-rich non-perovskite phases might arise as a result of excess lead oxide compositions was, until now, speculative, because the excess lead oxide was expected to evaporate during sintering.

2. Experimental procedures

2.1. Columbite pre-cursor methods

With many of the complex Pb-based perovskite-structured ceramics, conventional processing by mixed-oxide methods leads to the formation of

0022–2461/90 $03.00 + .12

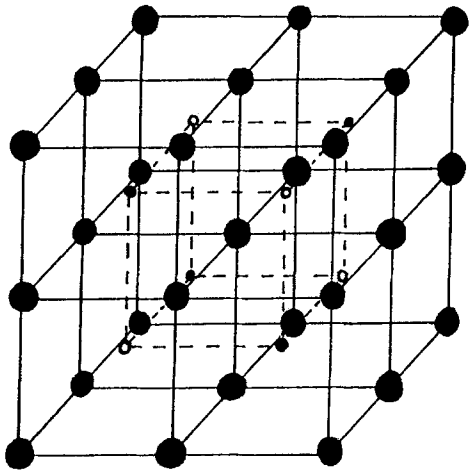

Figure 1 Structural model of ordered PST illustrating the relative positions of Pb, Sc and Ta in a 0.814 nm fcc ($2a_0\,2a_0\,2a_0$) unit cell. (● Pb, ● Sc, ○ Ta).

undesirable pyrochlore-type second-phases. Methods of inhibiting the formation of these phases were suggested by Swartz and Shrout [7] and Lejeune and Boilot [8]. In this process, a separate B-site precursor reaction takes place which results in the formation of Columbite or Wolframite-structured compounds. The method of pre-reacting the B-site cations to form Columbite phase is successful with the relaxor $Pb(Sc_{1/2}Ta_{1/2})O_3$, but with $Pb(In_{1/2}Nb_{1/2})O_3$ it is only partially successful [9]. It has been suggested that two parameters are important in the formation of a stable perovskite structure: the ionic radii of the cations and the attraction between the cation and anion. The ionic radii of the cations should lie within certain limits and the attraction between the cation and anion should be strong [10].

2.2 Compositions of samples

A homogeneous mixture of scandium oxide (Sc_2O_3) and tantalum oxide (Ta_2O_5) was initially produced by vigorously milling the two oxides in acetone. The mixture was subsequently subjected to calcination which resulted in the formation of a single phase compound as observed by X-ray diffraction (Equation 1)

$$Sc_2O_3 + Ta_2O_5 \rightarrow ScTaO_4 \text{ (Columbite)} \quad (1)$$

The $ScTaO_4$ was milled into a powder and then mixed with PbO in acetone. The resulting homogeneous mixture was subjected to calcination. This process can be represented by Equation 2.

$$ScTaO_4 + 2PbO + \text{excess PbO(5–10 wt \%)} \rightarrow Pb_2(ScTa)O_6 \text{ (perovskite)} \quad (2)$$

Excess PbO was added in order to prevent the formation of the parasite pyrochlore-structured phase during the final high-temperature steps. The $Pb_2(ScTa)O_6$ was again milled so that the powder could be cold-pressed into the required shape. The resulting green pellets were hot-pressed. The hot-pressing was carried out in an O_2-rich atmosphere. (The samples prepared will be abbreviated to P_5ST and $P_{10}ST$ where the subscripts represent 5 wt % and 10 wt % excess PbO, respectively).

2.3. Electron microscopy

Samples of PST were prepared for TEM investigations by conventional methods. The samples were initially cut with a diamond saw, and then ground to a thickness of approximately 30 μm using silicon carbide papers. A copper support grid was then glued onto the surface of each polished specimen using an epoxy resin. The supported disc of ceramic was subsequently "chipped" away from the surrounding material. Electron transparent regions were obtained by atom-beam milling the specimen using an Ion-Tech "fast atom" beam thinner which was operated at an accelerating voltage of 5 kV and at incidence angle of 18 to 25°. Specimens were then carbon-coated to prevent charging within the electron microscope. They were examined at 200 kV using Jeol-200CX and Philips EM430 transmission electron microscopes. Compositional data were obtained from the specimens using the Jeol-200CX which was equipped with a link energy dispersive X-ray detector and spectrum processing facilities (EDS).

3. Observations and discussion

3.1. Spheroidal inclusions in lead scandium tantalate

Fig. 2a is a bright-field electron micrograph which shows a circular inclusion within a crystallite in a hot-pressed sample of P_5ST. Extensive investigation of several grains, each in a different orientation with respect to the electron beam, did not reveal the presence of any acicular second phases. Therefore, it was concluded that the circular morphology arose as a result of the plane of the thin specimen cutting through a spherical particle. In addition, the finding of an acicular second-phase inclusion would have implied that it was a precipitate with a preferred crystallographic direction of growth. Such features have not been observed within this material.

Spheroidal inclusions constitute the commonest second-phases and are non-uniformly distributed within the perovskite ceramics. The spheroids are multiphase Pb-rich pockets of material which exist within individual grains and are isolated from other impurity phases (Fig. 2a). The presence of moiré fringes within the image of the spheroid indicates that there are at least two overlapping crystals within the spheroid. Fig. 2b is an energy dispersive of X-ray spectrum (EDS) obtained from the spheroid shown in Fig. 2a. It can be seen that the metallic content of the spheroid is almost entirely lead. It is possible that Pb-enrichment arises as a result of the entrapment of PbO at grain boundaries and within pores during the early stages of sintering and is concentrated by subsequent grain growth.

The spheroids exhibit extraordinary structural diversity. As indicated by Fig. 3a, they are often segmented and have complex microstructures that consist of interfaces, faults and small volume second-phase particles which give rise to strain field contrast (marked A in the micrograph). The parallel striations

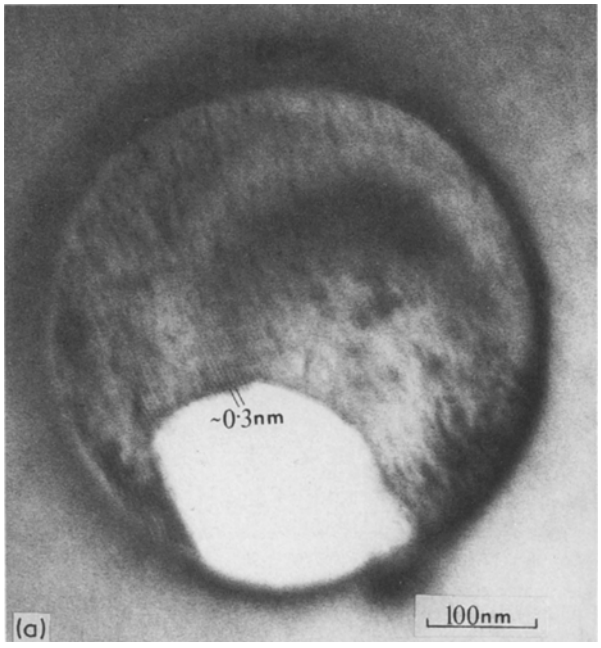

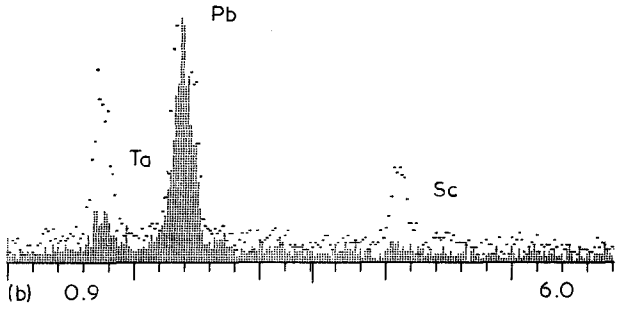

Figure 2 (a) Bright-field micrograph illustrating a spheroidal inclusion within a PST crystallite. Fine moiré fringes of spacings ~0.3 nm can be seen in the image of the spheroid. (b) EDS spectrum obtained from the spheroid of Fig. 2a shows that its metallic content is almost entirely Pb. The dotted lines represent the spectrum from a grain of PST obtained under similar microscope conditions.

observed within the segments of the spheroids are stacking faults. These defects could arise from polytypism, twinning or crystallographic shear within the crystall lattice [11].

It can be seen in Fig. 3a that the central segment of the spheroid contains fewer defects than the neighbouring segments. The high degree of lattice coherency can be assessed from the regular arrangement of the lattice fringes (d-spacings ~0.61 nm). Although the overall periodicity of the lattice fringes appears uninterrupted, a lattice image (in Fig. 3b), obtained under 30 μm defocus conditions, reveals that there are coherent precipitate particles present and exhibits slightly displaced lattice–plane fringes, marked A and B, respectively. The inset of Fig. 3b shows an enlarged view of the uninterrupted set of lattice–plane fringes (0.61 nm) present within both the precipitate and the

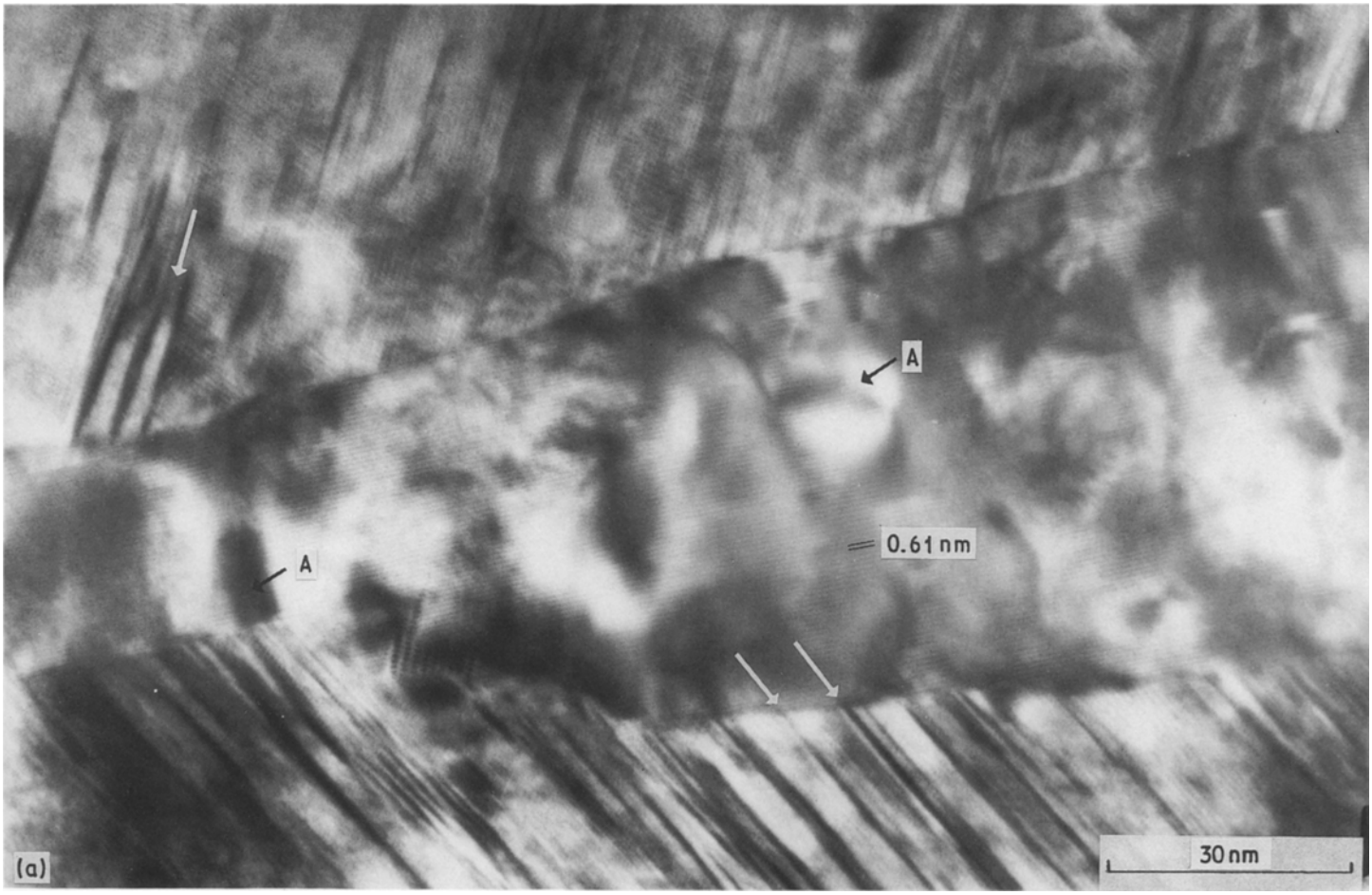

Figure 3 (a) Bright-field micrograph illustrating the complex microstructure of a Pb-rich spheroidal inclusion. The parallel striations (arrowed) represent extensive planar lattice disorder. (b) An enlarged view of the central segment of the spheroid of Fig. 3(a) illustrating strain field contrast (A), slightly distorted lattice–plane fringes (B) and moiré fringes (C). Inset: lattice–plane fringes illustrate the coherency of a second-phase particle/precipitate with the matrix.

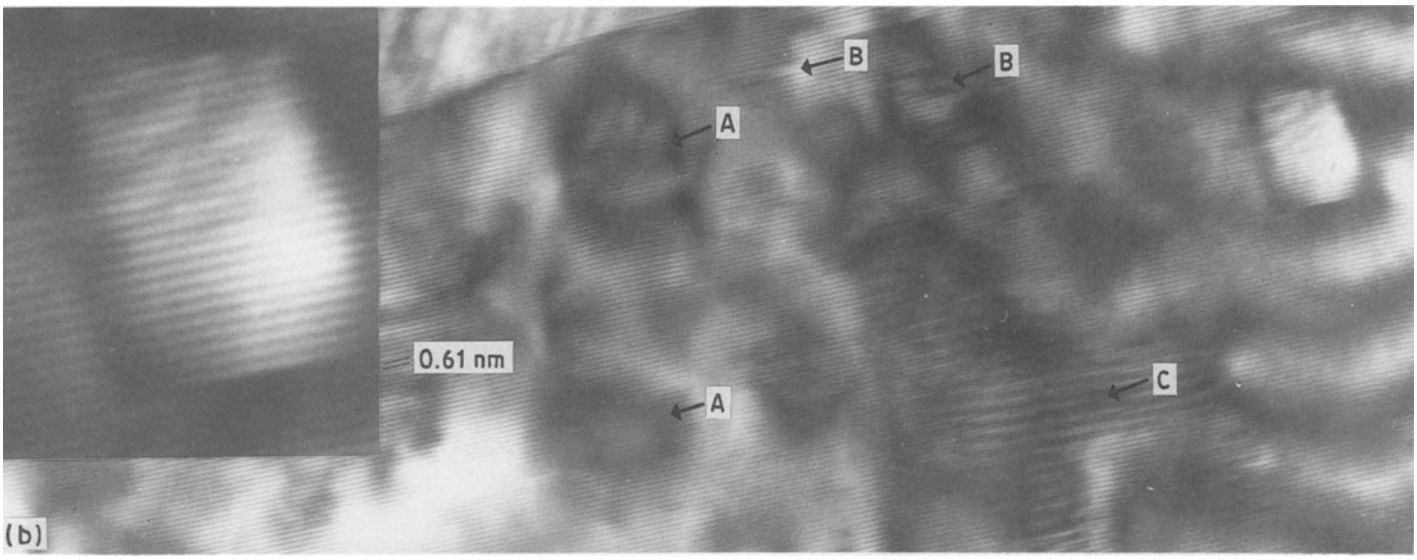

Figure 3 Continued.

matrix. These indicate that the precipitate is coherent with the matrix. The localized moiré fringes, with spacings ~ 1.5 nm (marked C in Fig. 3b), arise as a result of superposition of second-phase particles on a matrix with different lattice constants. It is likely that the irregularities observed within the moiré fringes originate from local lattice distortions. In addition, it is seen that patches of dark contrast dominate the microstructure. These dark patches originate from the strain field contrast induced by both the coherent and non-coherent second-phase particles and buckling of the specimen due to heating within the electron beam.

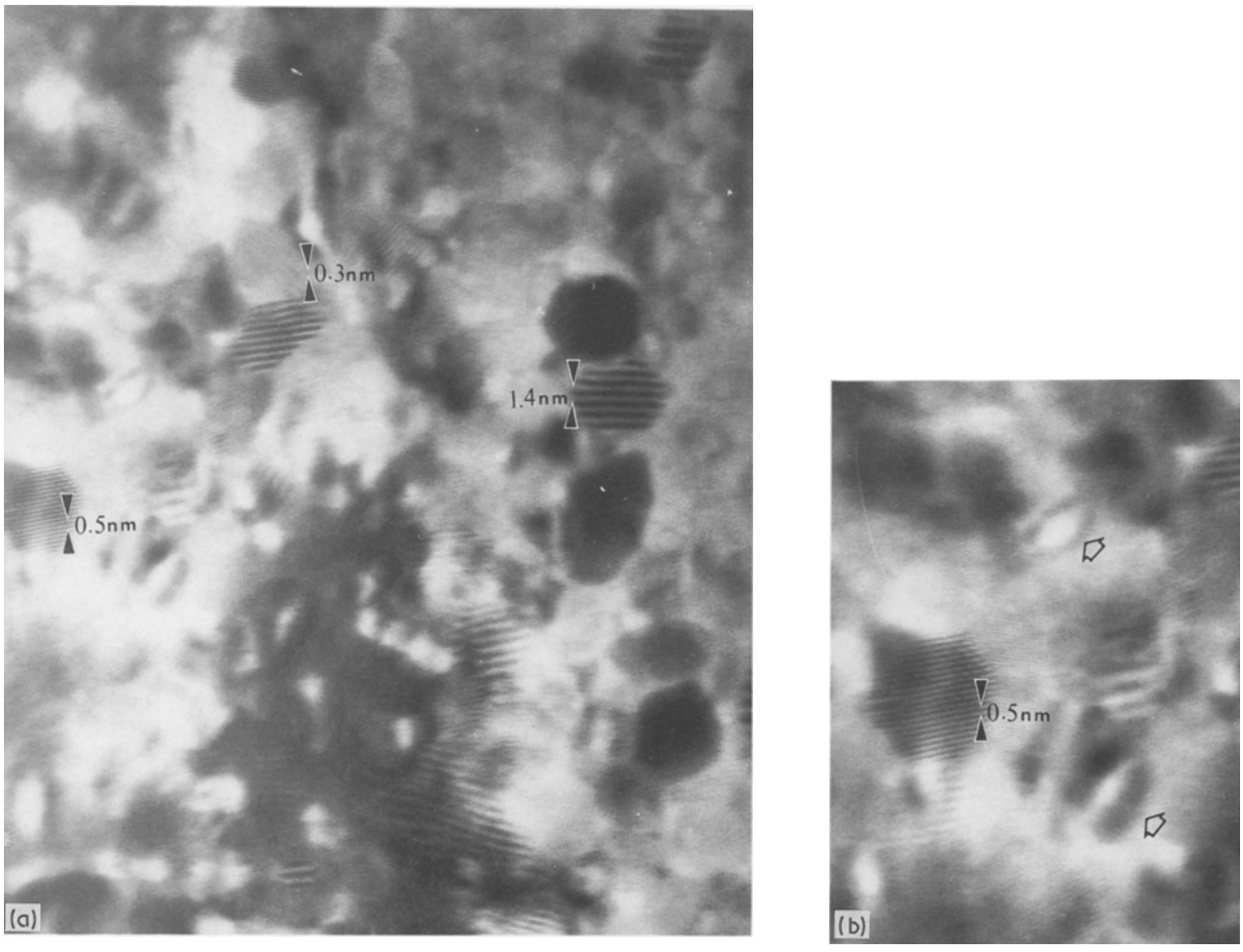

Figure 4 (a) Dark-field micrograph showing fine moiré fringes at the plate-like precipitates. (b) An enlarged dark-field micrograph showing moiré fringes associated with the plate-like precipitates. Strain field contrast can also be seen (arrowed). Such effects are probably caused by small volume precipitates present within the PST crystalline.

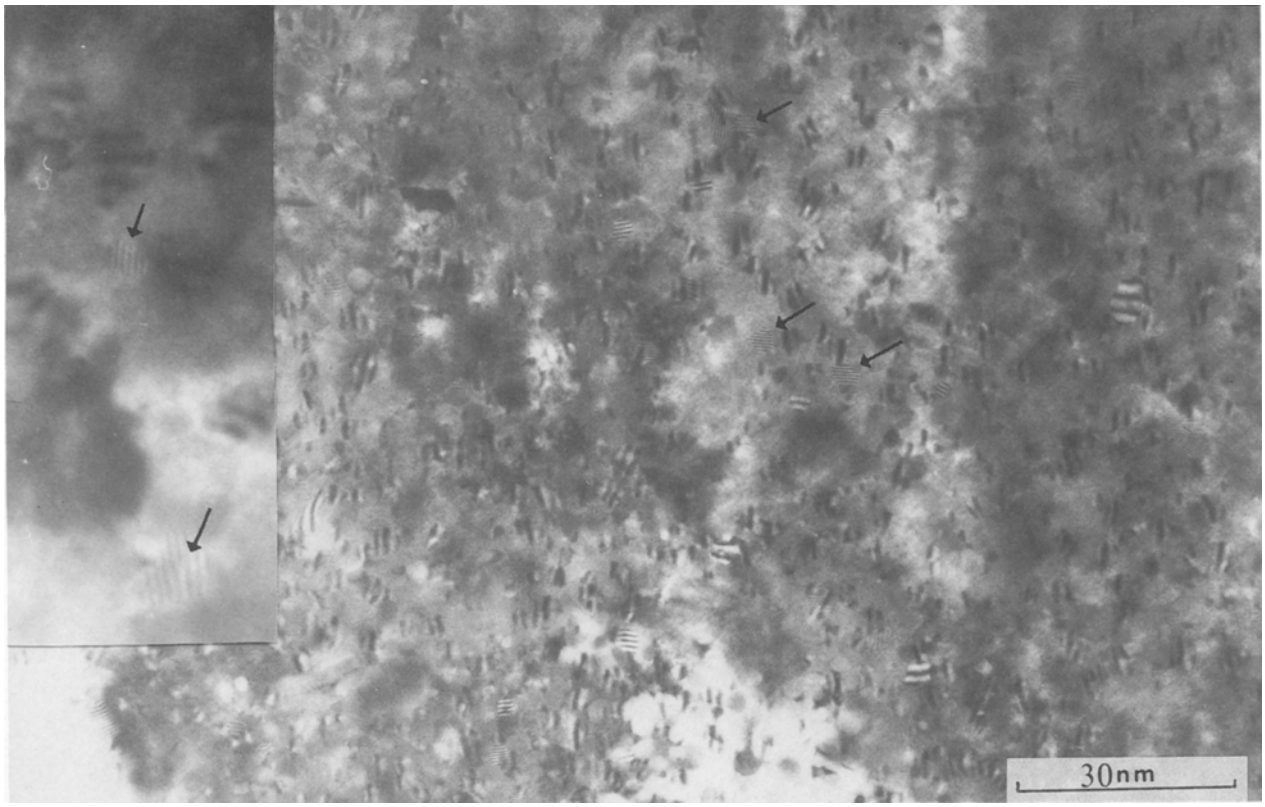

Figure 5 Dark-field micrograph showing extensive electron beam-induced defects in a crystallite of $P_{10}ST$ which contained plate-like precipitates. Moiré fringes can also be seen (arrowed). Inset: An enlarged view showing defects resulting from electron irradiation.

Preliminary investigation suggests that the crystal structure of the central segment of the spheroid is identical to that of Pb_3O_4 (space group $P4_2/m\,b\,c$, $a_0 = 0.882\,nm$, $c_0 = 0.657\,nm$). This phase could have been produced by the oxidation of small amounts of PbO during one of the high temperature processing stages used in fabricating the ceramic. In most cases, the crystal structures and the compositions of the spheroidal inclusions could not be reliably determined owing to their small sizes, and as a result it was impossible to ascertain the exact nature and cause of the faults in the crystals present within them.

3.2. Identification of plate-like precipitates by moiré patterns

It has been shown in Section 3.1. that second-phase particles can be recognized either because they diffract differently from the matrix grains or because they give rise to strain field contrast. However, the existence of second-phase particles within the matrix grains can also be revealed by their causing the formation of moiré fringes [12, 13]. By analysing fine-scale regions showing moiré fringes, it was possible to identify tiny plate-like precipitates distributed throughout the interior of some grains. An example from P_5ST is shown in Fig. 4a where moiré fringe spacings in the range 0.3 to 1.37 nm can be observed where small precipitates are present. The distortions observed in some of the fringes originate from lattice imperfections. In addition, there are examples of strain field contrast (marked by arrows in Fig. 4b) caused by small plate-like precipitates present within the crystallites which are more "edge-on" with respect to the direction of the electron beam.

It should be pointed out that small particles which are structurally coherent with the ceramic could easily be sputtered onto the PST specimens during atom-beam thinning. If such sputtered particles were sufficiently thin, then it would be possible for them to give rise to moiré fringes, provided that the $\boldsymbol{g}$-vectors of the diffracting planes of the PST grains and the superposed sputtered particles are either parallel and slightly dissimilar, or similar but mutually rotated through a small angle. Although it was not possible to eliminate the possibility that some particles had been deposited on specimen surfaces during atom-beam thinning, high densities of plate-like precipitates were consistently associated with several anomalous microstructural features which point to their being internal and intrinsic, i.e. they formed during grain growth; these include the following.

(a) The grains which contain plate-like precipitates are Pb-enriched. EDS microanalysis revealed an appreciable enhancement in the Pb content of the PST grains containing precipitates, compared with those without precipitates. However, reliable EDS microanalysis could not be carried out on individual precipitates because of their small size ($\sim 10\,nm$).

(b) The grains with precipitates showed extraordinary sensitivity to electron-beam irradiation. Whereas the normal grains were stable under the action of the electron beam, the grains with precipitates rapidly developed clusters of defects. It was observed that the sizes, shapes and numbers of the defects were

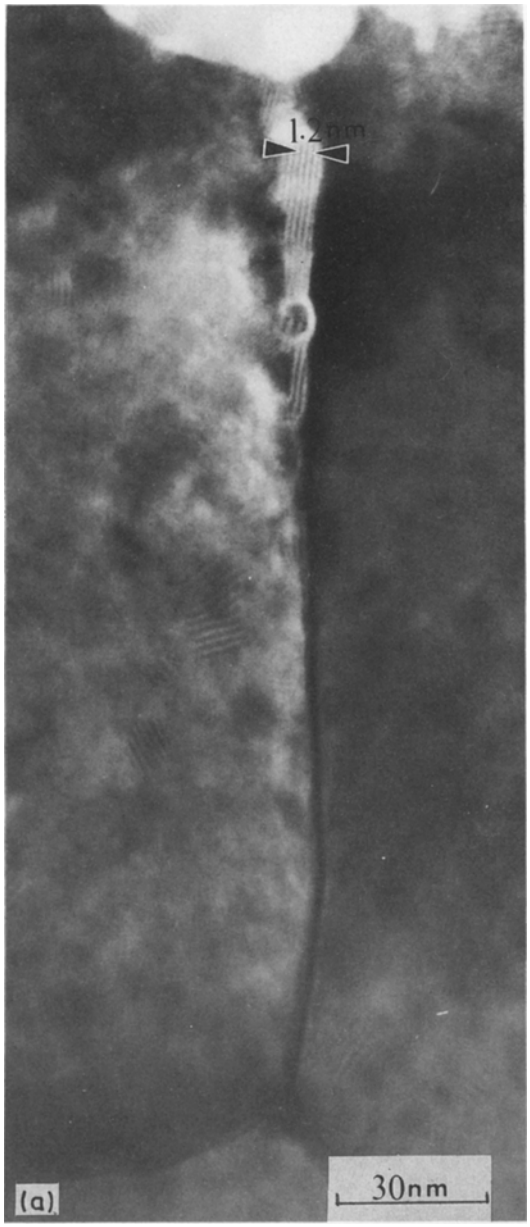

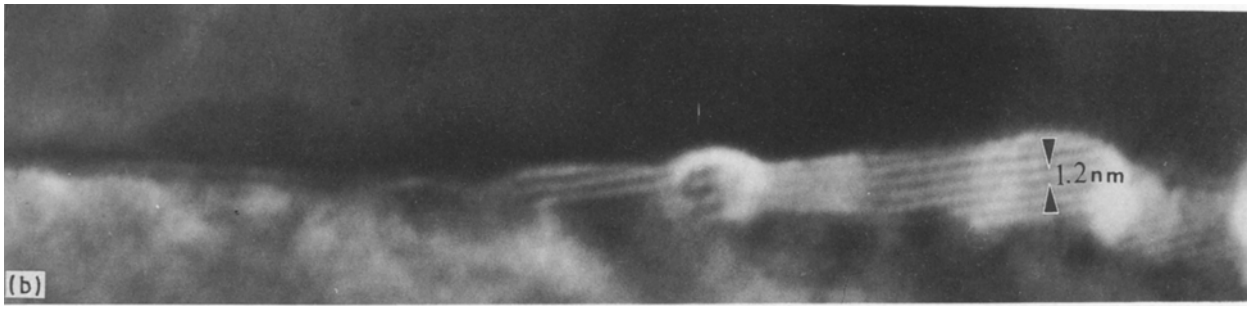

Figure 6 (a) Bright-field micrograph illustrating second-phase inclusions at a grain boundary and at the adjacent triple junctions. The presence of moiré fringes at the inclusion close to the triple junction indicates that the inclusion is crystalline. (b) An enlarged view illustrating the moiré fringes at the grain boundary inclusions.

determined by electron beam dose and duration of exposure. When the specimen temperature was gradually raised, dislocation loops were generated and frequently transformed, to give fringes similar to those exhibited by stacking faults. Also, prolonged exposure under a focused electron beam resulted in localized decomposition of the sample. An example from $P_{10}ST$ is shown in Fig. 5, where a high density of beam-induced defect clusters can be seen. A number of precipitates which exhibit moiré fringes can also be seen in Fig. 5. The inset of Fig. 5 shows an enlarged view of both the fault-fringes and moiré fringes. The former arise from displacements of the crystal lattice by the effects of electron beam irradiation.

The exact causes of plate-like precipitation in these materials could not be established. However, local Pb-enrichment indicates that the presence of plate precipitates can be linked to severe departures from stoichiometry. Elecron beam damage in the Pb-enriched regions is a good indication of non-stoichiometry and chemical instability. Similar effects have been reported in other oxide compounds, e.g. by Reece and Barber [14]. It is possible that small-volume precipitates, voids, vacancies and entrapped gas

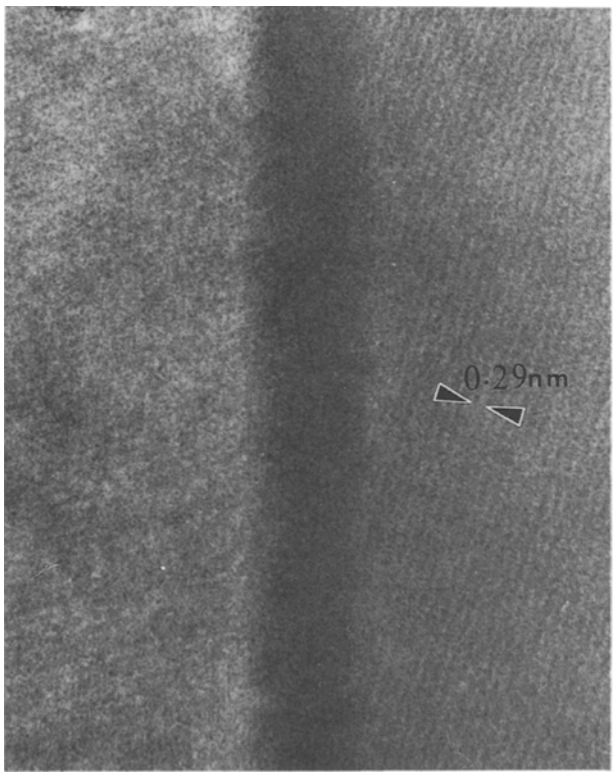

Figure 7 Lattice-plane fringes corresponding to the (1 1 0) planes in P_5ST in two grains separated by an intergranular impurity film.

bubbles combined with the presence of some liquid phase PbO, when exposed to the electron beam, give rise to the nucleation of clusters of defects.

(c) The presence of plate precipitates is also associated with unusually high levels of impurity at nearby grain boundaries and triple junctions. Fig. 6a illustrates submicron-sized inclusions at grain boundaries and a volume of second-phase close to the triple junction. The crystalline nature of the triple junction second-phase, shown enlarged in Fig. 6b, can be deduced from the presence of moiré fringes of spacing ~ 1.2 nm. EDS microanalysis of the triple junction phase revealed that this phase contained only traces of tantalum and scandium. The thickness of the second-phase close to the triple junction was approximately 10 nm and its thickness was observed to decrease as the distance from the triple junction increased. The inclusions at the grain boundaries adjacent to the triple junction are considerably thicker than the average integranular films ($\simeq 1$ nm) and are thought to be composed of partially amorphous PbO. It is interesting to note that in Fig. 6a the contrast of the intergranular boundary phase changes from white to black as the volume of phase reduces. Close to the triple junction the second-phase has light contrast and is crystalline because it exhibits moiré fringes; away from the triple junction the second phase exhibits dark contrast and moiré fringes are not apparent. Although it was not possible to establish whether dark contrast necessarily represents an amorphous phase, lattice imaging has shown that the thin intergranular phases exhibit dark-contrast and are frequently amorphous.

3.3. Non-perovskite intergranular in PST

We have seen in Section 3.2. that segregation can occur at grain boundaries and triple junctions in PST ceramics with high levels of impurity. Larger volumes of non-perovskite phases were observed at triple junctions in locations unaffected by the anomalous microstructural features discussed in Section 3.2. Moreover, several samples of $P_{10}ST$ and P_5ST ceramics that we have investigated (both annealed and unannealed) exhibited thin amorphous films at their grain boundaries.

Lattice imaging can be used [15, 16] to observe thin intergranular films and to investigate their morphology. In Fig. 7, the discontinuities in the (1 1 0) lattice-plane fringes ($d_{110} = 0.288$ nm) at the interface between two neighbouring crystallites in unannealed P_5ST indicate the presence of a very thin amorphous intergranular phase. The thickness of the film was estimated to be ~ 1.5 nm and its amorphous character was deduced from its failure to diffract. Further observations utilizing the (1 1 0) lattice-plane fringes showed that the thickness of the intergranular film was not uniform throughout the boundary. The composition of the intergranular film could not be reliably determined using the available EDS facilities, but it is very likely that excess PbO segregates preferentially at grain boundaries and triple junctions.

In addition to the very thin amorphous phases (1 to 3 nm in thickness) that were often imaged with the aid of lattice fringes, larger volumes of Pb-rich crystalline phases were observed within some triple junctions in both the annealed and unannealed P_5ST ceramics. Fig. 8a is a bright-field electron micrograph illustrating a predominantly Pb-rich non-perovskite triple-junction phase in annealed P_5ST. The microstructure of this phase is inhomogeneous owing to the presence of precipitates and defects. The fringes in the image appear to arise from both stacking faults and overlapping lattices. The selected area diffraction pattern (SADP) obtained from this phase is rather complex because it not only contains reflections originating from precipitates, but it also exhibits distorted and shifted matrix reflections which indicate the presence of lattice disorder (Fig. 8b). However, careful inspection reveals two systematic rows of reflections labelled with arrows. The individual reflections marked g_1 and g_2 represent interplanar distances of 0.49 and 0.30 nm, respectively. These values closely correspond to the interplanar distances of 0.51 and 0.28 nm of the (0 0 1) and (1 1 0) reflections in PbO. Thus, the zone axis represented by the SADP can be indexed as $[\bar{1}\,1\,0]$. PbO has a space group $P4/nmm$ which permits all orders of reflections except $hk0$ with $h + k = 2n$. Based on this space group, the reflections g_1 and g_2 can also be indexed as (0 0 1) and (1 1 0), respectively, which yield the lattice constants $a_0 = 0.49$ nm and $c_0 = 0.41$ nm. These values closely correspond to the actual lattice constants $a_0 = 0.50$ nm and $c_0 = 0.41$ nm.

It is interesting to recall that PbO, as well as being used as a precursor compound during the initial stages of fabrication, is used in excess as a wetting agent to aid in the densification process and to compensate for PbO loss. Although PbO can remain within the PST ceramics as a consequence of poor mixing and incomplete reaction, it is likely that the particles second-

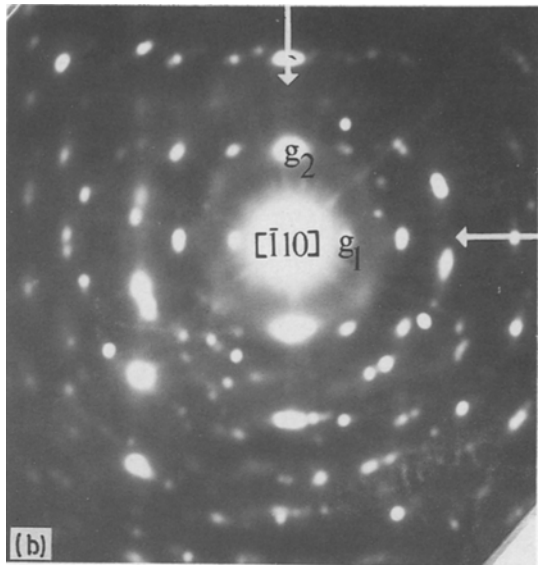

Figure 8 (a) Bright-field micrograph of a Pb-rich second-phase inclusion at a triple junction. The dark patches of contrast present in the micrograph originate from the effects of electron-beam irradiation. (b) SADP corresponding to the second-phase inclusion of Fig. 8a.

phase observed at the grain boundaries and triple junctions originated from excess PbO, which became entrapped during grain growth and sintering.

4. Precipitation in P_5ST prepared by a sol process

Figs 9a and b are bright field TEM micrographs which show perovskite-structured grains that contain second-phase particles. The particles lie in the grain interior. Some particles are faceted, which implies that the second-phase is crystalline while some particles exhibit moiré fringes caused by the superposition of dissimilar lattices. The majority of perovskite grains contain a small volume fraction of this second-phase, but the total volume fraction is difficult to ascertain. Electron diffraction partterns could not be obtained from the particles owing to their small sizes and electron diffraction patterns from perovskite grains which contained a large volume fraction of particles did not reveal simple orientation relationships to the PST grains. However, high resolution electron microscopy was carried out on a sample of P_5ST and this revealed that some particles were coherent with the matrix grains (and presumably precipitated from solid solution at high temperature) (see Fig. 9c).

Fig. 10 is a transmission electron micrograph of a pore within a perovskite grain. This contains an amorphous spheroidally-shaped phase which was sensitive to the electron beam. The defects which can also be observed in the micrograph are dislocations that connect to the pore. It is believed that the amorphous spheroidal-phase is excess PbO which has not volatilized during the manufacturing process. Fig. 11 is a TEM micrograph which shows a coarse dislocation network within a PST grain. Dislocations occur only rarely in these sintered ceramics and their tendency to be associated with pores merely indicates that entanglement has occurred during the sintering and grain growth.

Fig. 12a is an electron diffraction pattern from another perovskite grain with the electron beam parallel to the [1 1 0]. The intense Bragg reflections can be indexed according to a primitive cubic Bravais lattice (a_0 = 0.41 nm unit cell). The weaker {1/2 1/2 1/2} reflections arise from a fcc superlattice ($2a_0\,2a_0\,2a_0$) which is produced by the ordering of Sc and Ta atoms on the B-site lattice. Dark-field images obtained using {1/2 1/2 1/2} reflections revealed a complex distribution of ordered domians throughout the PST grain, as typified by Fig. 12b. Fig 13a and b are, respectively, enlarged bright- and dark-field images of the grain shown in Fig. 12b. A comparison of the two reveals an increase in the number of ordered domains at the precipitate/matrix interfaces. It is proposed that the presence of an interface or planar defect facilitates the nucleation of the ordered domains. This implies that an increase in the volume fraction of second-phase would effect the degree of ordering of atoms on the B-site lattice. Fig. 14 is a bright-field high-resolution electron micrograph imaged with the electron beam parallel to the [1 1 0] which shows the boundary between a disordered region of perovskite PST(A) and an ordered region (B). The change from disorder to order across the micrograph is associated with an increase in the contrast of every second fringe (d = 0.23 nm). The increase in contrast arises as a result of the superposition of the {1/2 1/2 1/2} superlattice

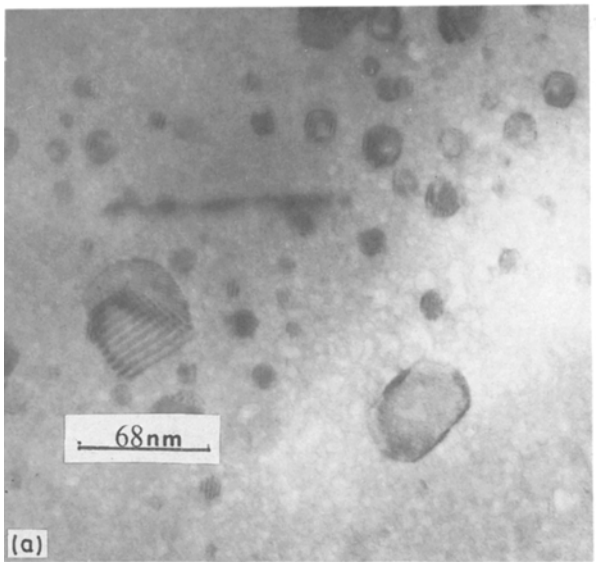

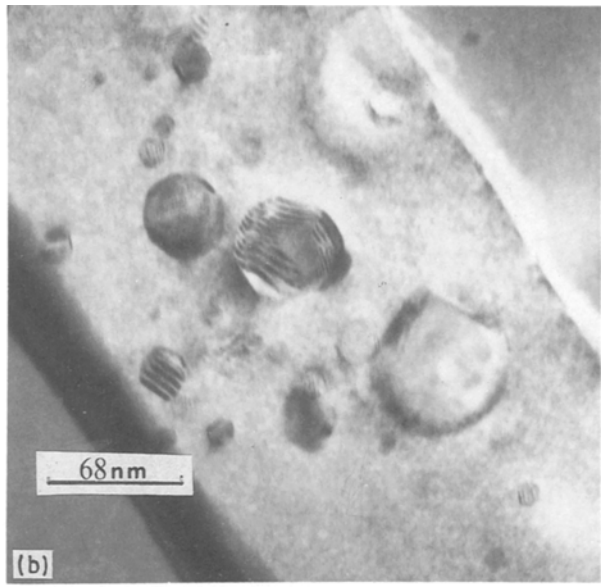

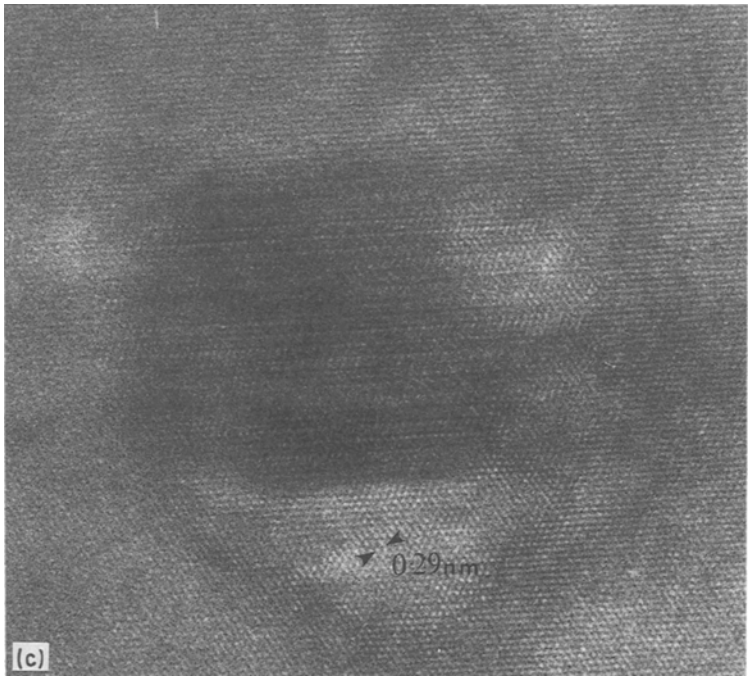

Figure 9 (a) and (b) Micrographs showing second-phase particles present within the PST grains. Moiré fringes can be observed where particles are present in the matrix PST grains. (c) High resolution micrograph of a coherent precipitate imaged with the electron beam parallel to the [1 1 1] (d_0 = 0.20 nm). The dark fringes within the precipitate have a d-spacing of approximately 0.5 nm.

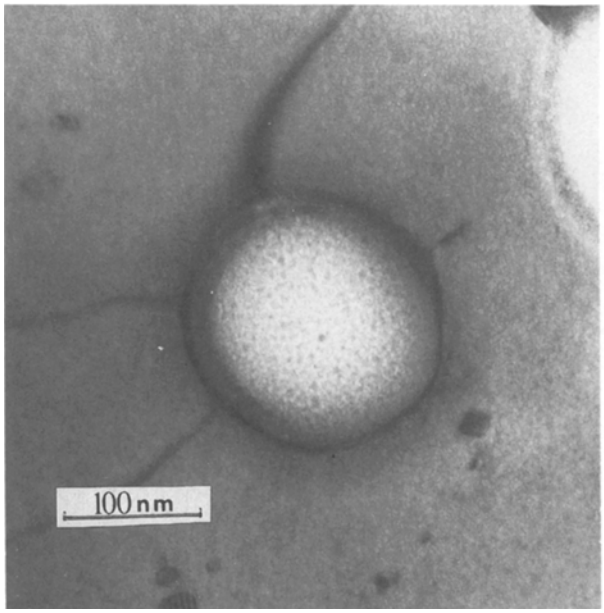

Figure 10 Micrograph showing a pore filled by lead oxide within a PST grain. Dislocations can be observed connecting to the pore.

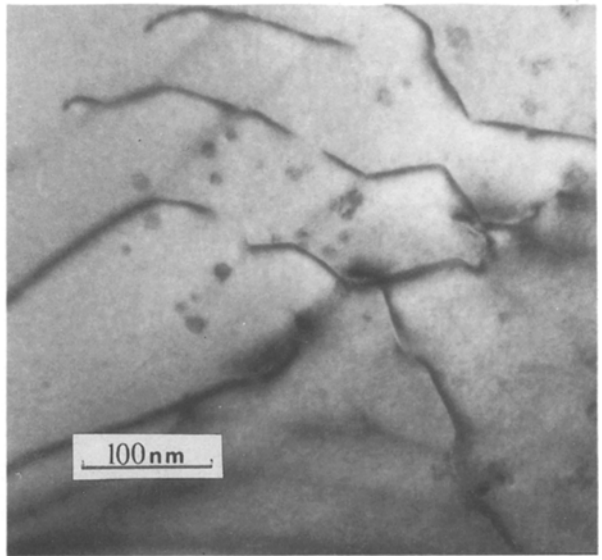

Figure 11 Micrograph illustrating part of a coarse dislocation network within a PST grain.

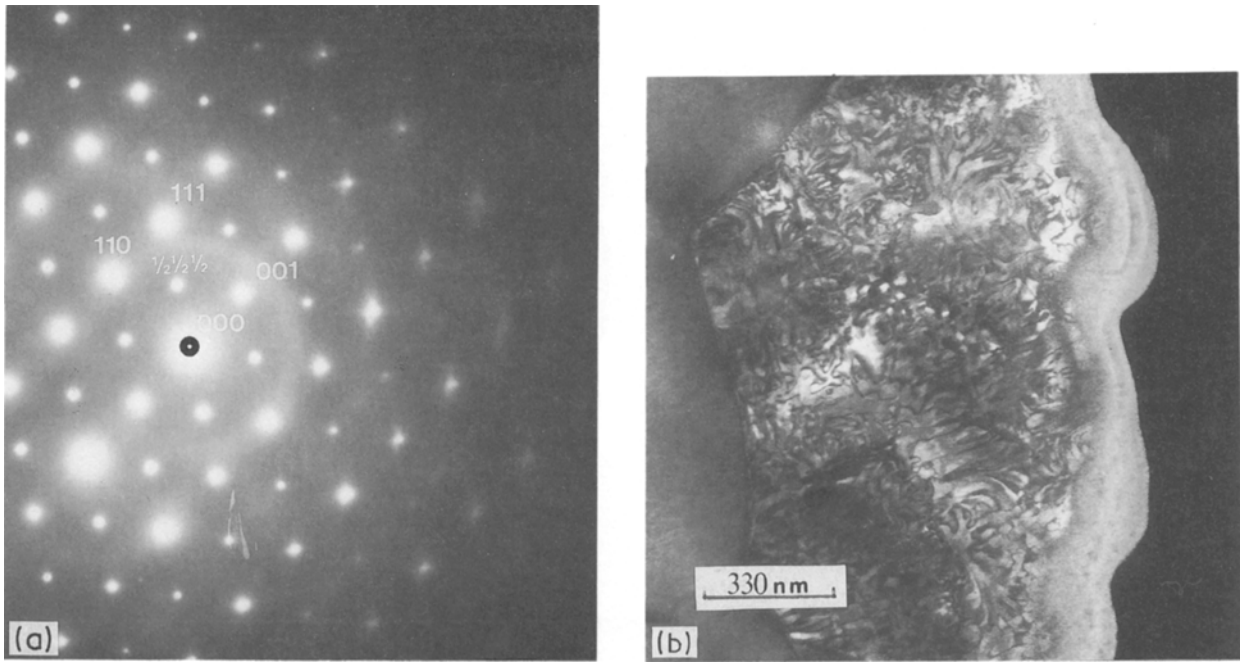

Figure 12 (a) Electron diffraction pattern with the electron beam parallel to the [1 1 0]. The {1/2 1/2 1/2} superlattice Bragg reflection can be observed in the pattern. (b) Dark-field electron micrograph obtained using a {1/2 1/2 1/2} Bragg spot.

reflection into every second [1 1 1] matrix reflection. The area marked (C) on the micrograph is an adjacent grain: the electron beam was not parallel to a high order zone axis.

5. Conclusions

Using TEM methods, it has been possible to identify various and diverse types of Pb-rich second-phases within ceramic samples of the ferroelectric, lead scandium tantalate. The results suggest that PbO additives become entrapped within the materials during fabrication, thereby generating the Pb-rich phases. There are at least two structural types: (a) amorphous or partially amorphous phases; (b) crystalline phases that do not have the perovskite structure. Such materials, although present in relatively small volumes, undoubtedly prevent the achievement of optimum dielectric properties. Amorphous or glassy phases that are non-ferroelectric are dispersions of a low permittivity material in the high permittivity matrix, thus acting as a 'dielectric dilutant'. Their occurrence as films along grain boundaries must also attenuate grain-to-grain dipole coupling, presumably having implications for both switching behaviour and dielectric loss. Second-phase inclusions within grains prevent the formation of regular FE domain configurations and also tend to give domains a 'memory'

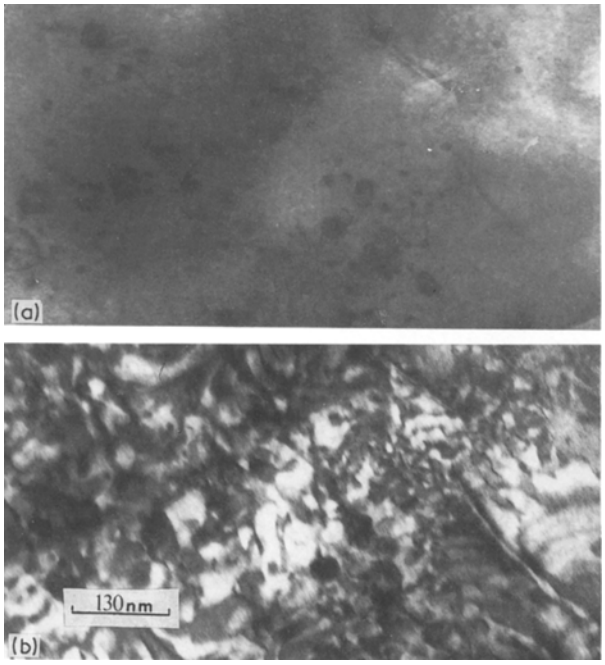

Figure 13 Micrographs showing (a) bright-field image of a perovskite grain and (b) the corresponding dark-field image obtained using a {1/2 1/2 1/2} Bragg spot.

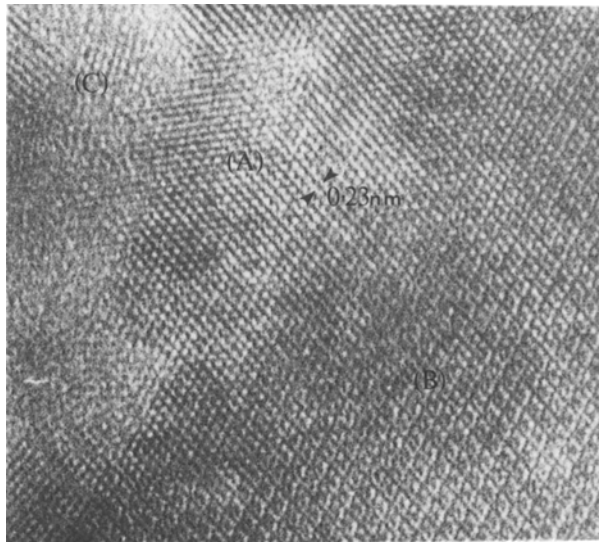

Figure 14 High resolution electron micrograph of an ordered domain obtained with the electron beam parallel to the [1 1 0] and the objective aperture enclosing both the sub-lattice and superlattice reflections. The dark fringes arise as a result of the superposition of {1/2 1/2 1/2} superlattice reflections onto every second {1 1 1} reflection.

in switching. Defect-induced heterogeneities in the degree of structural order imply local variations in the dielectric permittivity of the perovskite-structured matrix grains and will contribute to dielectric loss because of the relationship between the degree of order and relaxor behaviour [17, 18].

Acknowledgements

The authors would like to thank Dr R. Whatmore and Mr P. Osbond for supplying materials and for useful discussions concerning the fabrication of the ceramics. Support from SERC/MoD grant XG10596 is gratefully acknowledged.

References

1. G. A. SMOLENSKY, *J. Phys. Soc. Jpn* **28** (1970) 26.
2. C. G. F. STENGER and A. J. BURGGRAAF, *Phys. Status. Solidi* (a) **61** (1980) 653.
3. C. G. F. STENGER, F. L. SCHOLTEN and A. J. BURGGRAAF, *Solid State Commun.* **32** (1979) 989.
4. C. A. RANDALL, D. J. BARBER, R. W. WHATMORE and P. GROVES, *J. Mater. Sci.* **21** (1986) 4456.
5. N. SETTER and L. E. CROSS, *J. Appl. Phys.* **51** (1980) 4356.
6. K. Z. BABA-KISHI, C. A. RANDALL and D. J. BARBER, Institute of Physics Conference Series No. 90: EMAG 87, 323.
7. S. L. SWARTZ and T. R. SHROUT, *Mater. Res. Bull.* **17** (1982) 1245.
8. M. LEJEUNE and J. P. BOILOT, *Ceram. Int.* **8** (8) (1982) 8, 99.
9. P. GROVES, *Ferroelectrics* **65** (1986) 67.
10. F. S. GALASSO, "Structure, Properties and Preparation of Perovskite-type Compounds" (Pergamon, New York, 1969).
11. S. AMELINCKX and J. VAN LANDUYT, "Diffraction and Imaging Techniques in Material Science", edited by S. Amelinckx, R. Gevers and J. Van Landuyt (North Holland, Amsterdam, 1978), 107.
12. P. B. HIRSCH, A. HOWIE, R. B. NICHOLSON, D. W. PASHLEY and M. J. WHELAN, "Electron Microscopy of Thin Crystals" (Butterworths, London, 1965).
13. E. C. ECOB and W. M. STOBBS, *J. Microsc.* **129** (1983) 275.
14. M. J. REECE and D. J. BARBER, *J. Mater. Sci.* **7** (1988) 649.
15. K. E. W. GOO, K. M. RAJA and G. THOMAS, *J. Amer. Ceram. Soc.* **64** (1981) 517.
16. D. R. CLARKE, *Ultramicroscopy* **4** (1979) 33.
17. SETTER and CROSS, *J. Appl. Phys.* **51** (1980) 8.
18. STENGER and BURGRAAF, *Phys. Status. Solidi* (a) **61** (1980) 275.

Received 3 November 1988
and accepted 14 April 1989